

Article

Effects of Specimen Thickness and Non-Isothermal Process on Creep Behavior of AA2024 Aluminum Alloy

Xintong Wu^{1,2,*} , Lihua Zhan^{2,3} , Youliang Yang^{2,3}, Yongqian Xu^{2,3}, Qiliang Zhang^{4,*} and Xiaobo Yang^{2,4}¹ School of Advanced Manufacturing, Nanchang University, Nanchang 330031, China² State Key Laboratory of High-Performance Complex Manufacturing, Central South University, Changsha 410083, China³ School of Mechanical and Electrical Engineering, Central South University, Changsha 410083, China⁴ College of Mechanical and Electrical Engineering, Lanzhou Jiaotong University, Lanzhou 730070, China

* Correspondence: wuxintong@ncu.edu.cn (X.W.); zql@mail.lzjtu.cn (Q.Z.)

Abstract: Fiber metal laminate (FML) is a kind of lightweight material that has garnered much attention in recent years due to its excellent properties under tensile, flexure, and impact conditions. However, little attention has been paid to the evolution of aluminum alloy during the FML forming process. In this paper, the effects of specimen thickness and the non-isothermal process on creep behavior of AA2024 aluminum alloy, which is generally used in FMLs, were systematically studied in terms of creep strain, mechanical properties, and microstructure. The results show that the microstructure and mechanical properties of the aluminum alloy layer are greatly affected by the creep age during the FML forming process, but the specimen thickness has little effect on the creep behavior under experimental conditions. During the non-isothermal process, the creep strain generated during the heating stage is about 40% of total strain. Compared with the isothermal process, the creep strain of the non-isothermal process increases by 20–40%, and the apparent activation energy Q_c is larger. According to the creep behavior of AA2024 aluminum alloy during the non-isothermal process, a creep constitutive model was established to accurately simulate the deformation of FMLs.

Keywords: AA2024 aluminum alloy; thickness effect; creep age forming; microstructure; non-isothermal constitutive modeling



Citation: Wu, X.; Zhan, L.; Yang, Y.; Xu, Y.; Zhang, Q.; Yang, X. Effects of Specimen Thickness and Non-Isothermal Process on Creep Behavior of AA2024 Aluminum Alloy. *Metals* **2023**, *13*, 409. <https://doi.org/10.3390/met13020409>

Academic Editors: Babak Shalchi Amirkhiz and Tomoyoshi Maeno

Received: 28 November 2022

Revised: 1 February 2023

Accepted: 13 February 2023

Published: 16 February 2023



Copyright: © 2023 by the authors. Licensee MDPI, Basel, Switzerland. This article is an open access article distributed under the terms and conditions of the Creative Commons Attribution (CC BY) license (<https://creativecommons.org/licenses/by/4.0/>).

1. Introduction

Lightweight materials are increasingly used in transportation, especially in aviation [1,2]. These kinds of materials can effectively reduce the weight and ensure the reliability and safety performance of structures so as to improve aircraft efficiency and reduce energy consumption and emissions. Fiber metal laminates (FMLs), as representatives of lightweight materials, are hybrid laminates consisting of extremely thin aluminum layers and fiber reinforced plastic. Their application in aviation has attracted more and more attention due to high impact resistance, great fatigue resistance, high damage tolerance, and other excellent performance [3,4]. In recent years, researchers have not only studied the properties of FMLs [5,6] but have also proposed novel methods for forming components, which lays a foundation for the promotion and application of FMLs [7,8]. A self-forming technique was developed for the manufacture of large curved skin panels, which is the key technology of FML forming at present [9]. This technique is very similar to the layup processes of composite structures, which require a high-temperature and high-pressure environment [10].

However, during the forming process, the forming temperature of FMLs coincides with the aging temperature of the aluminum alloy [11–13]. Therefore, the creep age of aluminum alloy is inevitable during the forming process. As for the creep behavior of aluminum alloys, researchers have conducted long-term research on the mechanism and theory [14–16], but the creep behavior of aluminum alloy during the forming process of FMLs has not attracted much attention. Compared with creep age forming of aluminum

alloys, the process of FMLs is quite different, in that it has a shorter time and a complex temperature change. Moreover, aluminum layers used for FMLs are mostly very thin plates with thicknesses of 0.3 mm or less, but research on creep age of metals mainly focuses on specimens with a thickness of around 1.5 mm [17–19]. The thickness effect of metal materials has always been the focus of researchers. In the 1970s, S. Floreen [20] studied the creep fracture properties of nickel-base superalloy specimens with different thicknesses. It was found that thickness had no significant effect in terms of failure time, crack growth, or failure mode, but W. Mills et al. [21] reported that fatigue crack growth rate retardation increased with decreasing specimen thickness in 2024-T3 aluminum alloy. S. Mahmoud et al. [22] and A. Asserin et al. [23] also found that the crack tip opening angle and fracture mode of aluminum alloys were affected by different thicknesses. However, the effect of specimen thickness on the characterization and evaluation of creep age has not been thoroughly evaluated. Therefore, it is necessary to determine the thickness effect on creep age behavior so as to gain a better understanding of the deformation of FMLs during the manufacturing process.

Furthermore, more and more researchers have begun to realize the importance of creep problems on experiments and simulations of FMLs. M. Prindera et al. [24] first investigated the time-dependent response of FMLs under creep loading, and then Vahid Daghigh et al. [25] tested the creep failure time, initial strain, and creep strain rate of basalt FMLs and studied the effect of temperature on creep behavior. M. Abouhamzeh et al. [26] developed a new procedure for small and large deformation analysis to try to predict residual stress in FMLs. However, there are few reports associated with the creep behavior of aluminum alloys in FMLs. So far, a thin aluminum alloy creep constitutive model suitable for FMLs has not been established for simulation analysis.

In order to provide some references for the FML manufacturing process, we studied the effects of specimen thickness and non-isothermal process on creep behavior of AA2024 aluminum alloy during FML forming. The results showed that the creep of AA2024 aluminum alloy in the non-isothermal FML-forming process was significantly increased under different applied stresses. Furthermore, we established a mechanism-based constitutive model describing the non-isothermal creep process. We anticipate the obtained constitutive model to be very promising for the FML manufacturing process.

The aim of this paper is to study the effects of specimen thickness and the non-isothermal process on the creep behavior of AA2024 aluminum alloy during FML forming. First, the thickness effects on creep and mechanical properties of AA2024 aluminum alloy are revealed by microstructural evolution. Then, creep behaviors of AA2024 aluminum alloy in the non-isothermal forming process of FMLs are investigated under different applied stresses. Furthermore, a mechanism-based constitutive model describing the non-isothermal creep process is established and compared with experimental results.

2. Material and Experimental

2.1. Materials

AA2024 aluminum alloy, which is widely used in FMLs, was selected in this study. For comparison, the thicknesses of specimens were selected to be 0.3 mm and 1.5 mm. The composition of aluminum alloy was 4.28Cu–1.20Mg–0.57Mn–0.037Fe–0.025Zn–0.01Ti–0.001Cr–0.078Si–(bal)Al (mass fraction, %). In agreement with the GB/T 2039-2012 standard, the specimens were machined out along the longitudinal direction of the as-received sheet, as shown in Figure 1. Then the specimens were solution-treated for 30 min at 773 K in a resistance furnace and subsequently water quenched at room temperature, followed by natural aging of the specimens

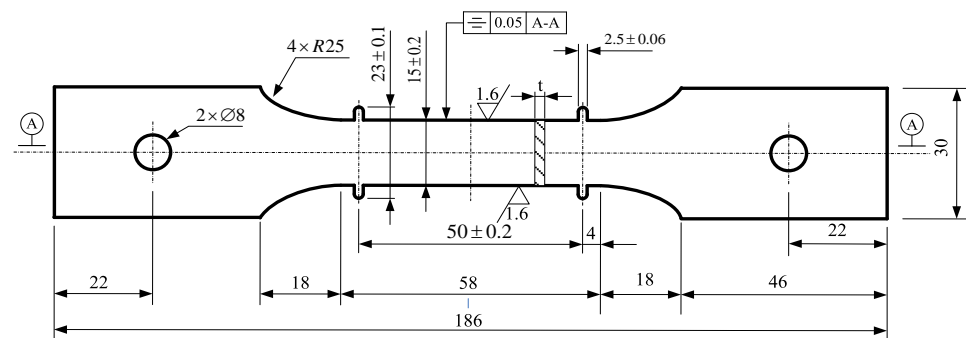


Figure 1. Drawing of creep age specimen adopted, in agreement with GB/T 2039-2012 (unit: mm).

2.2. Treatment

According to the creep-forming process of aluminum alloy, the isothermal creep age process temperature was selected at 453 K. The stress levels were selected as 90 MPa, 120 MPa, and 150 MPa, respectively, and the aging time was 12 h [27,28]. The non-isothermal process conditions referred to the FML curing process setting, as shown in Figure 2, and the stress levels were identical to those of the isothermal process. The creep age treatment was conducted on an RMT-D10 electron creep slackness tester, which guaranteed temperature deviation within ± 2 K during loading. According to the GB/T 228.1-2010 standard, tensile tests were performed on specimens after different creep processes at room temperature on an MTS Exceed E45 type testing machine with a loading speed of 2 mm/min. For each state, five horizontal samples were taken.

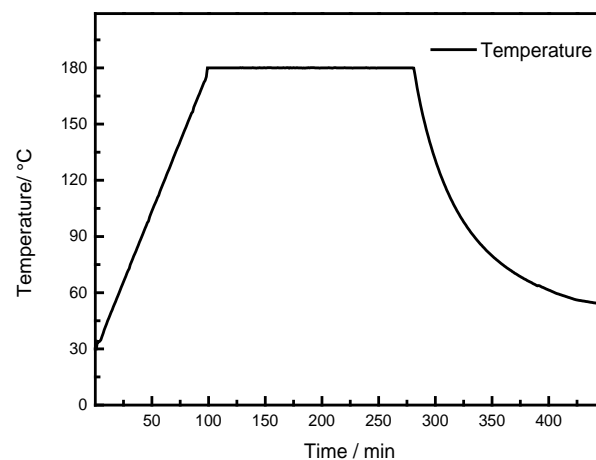


Figure 2. Non-isothermal temperature process curve.

2.3. Microstructural Analysis

The tensile fracture surfaces of the specimens after different creep processes were analyzed using a TESCAN scanning electron microscope. The specimens for transmission electron microscope (TEM) observation were first thinned to 80 μm by mechanical polishing and then electro-polished using twin-jet equipment with a voltage of 15 V. A mixture solution of 30% nitric acid and 70% methanol was used for electro-polishing at -30 °C. Finally, the specimens were cleaned with ethanol at room temperature for at least 5 min. TEM specimens were examined on a Tecnai G2 20 TEM machine operated at 200 kV.

3. Thickness Effect on the Creep Behavior of AA2024 Aluminum Alloy Applied in FMLs

3.1. Creep Strain Behavior

Figure 3 demonstrates the creep strain curves of AA2024 aluminum alloy with different thicknesses under conditions of different temperatures and stress levels. It can be clearly

seen that all creep curves exhibit typical features of the primary creep stage and steady-state creep stage, and the creep strain increases with time. The creep behaviors of AA2024 aluminum alloy with different thicknesses were compared, showing similar creep strains and trends. Under different stress conditions, the total creep strain difference between two specimens was not more than 5.35%. At a stress of 150 MPa for 12 h, the total creep strain of the specimen with a thickness of 0.3 mm was 0.142%, and the specimen with a thickness of 1.5 mm was 0.146%. Furthermore, their creep strain rates in the primary and steady-state creep stages were also similar, and the maximum creep strain rate difference was 4.47%, as seen in Figure 4. The results show that the creep strain of the specimens with different thicknesses was almost the same, indicating that the specimen thickness had no significant effect on the creep strain. This could be attributed to the fact that the creep strain is mainly determined by the applied stress and temperature, and the thickness of the specimen has little influence on the creep strain.

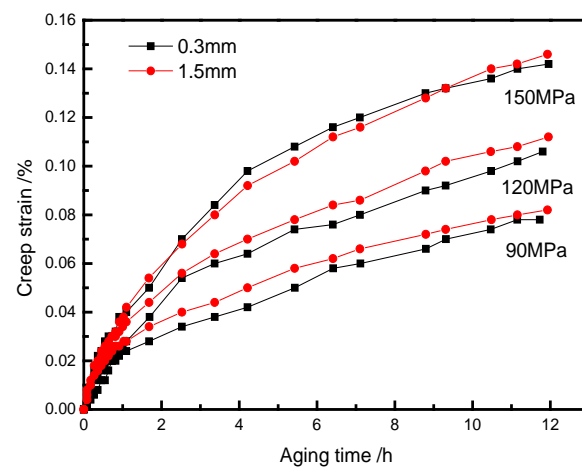


Figure 3. The comparisons of creep strain curves between 0.3 mm and 1.5 mm AA2024.

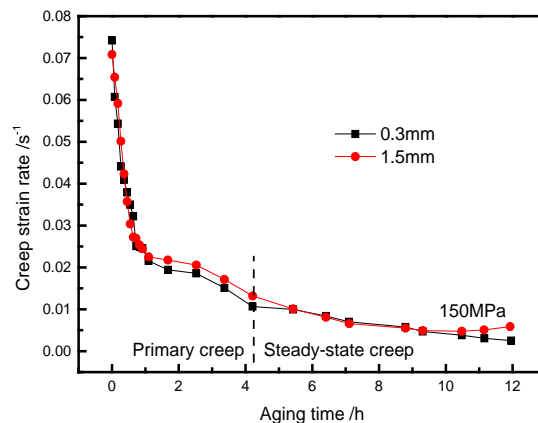


Figure 4. The comparisons of creep strain rates curves between 0.3 mm and 1.5 mm AA2024 at 453 K under stress of 150 MPa.

3.2. Mechanical Properties

Figure 5 presents the mechanical properties of AA2024 aluminum alloy with different thicknesses after different creep age processes. It is obvious that the mechanical properties of the aluminum alloy increased significantly after creep age, and especially the yield strength increased more than 70 MPa. With the increase of stress levels, the tensile strength and the yield strength increased and then decreased slightly. When the stress level was 90 MPa, the tensile strength reached its peak value. The thickness of the 0.3 mm specimen was 471.4 MPa, and that of the 1.5 mm specimen was 459.1 MPa. However, the elongation decreased significantly with the increase of stress levels, particularly in the specimen with

a 1.5 mm thickness. Comparing the mechanical properties, there were some distinctions between the specimens with different thicknesses. However, the variation trend of specimens was the same under any of the same conditions, which may have been due to the difference in the mechanical properties of the initial materials rather than the changes of materials in the creep age process.

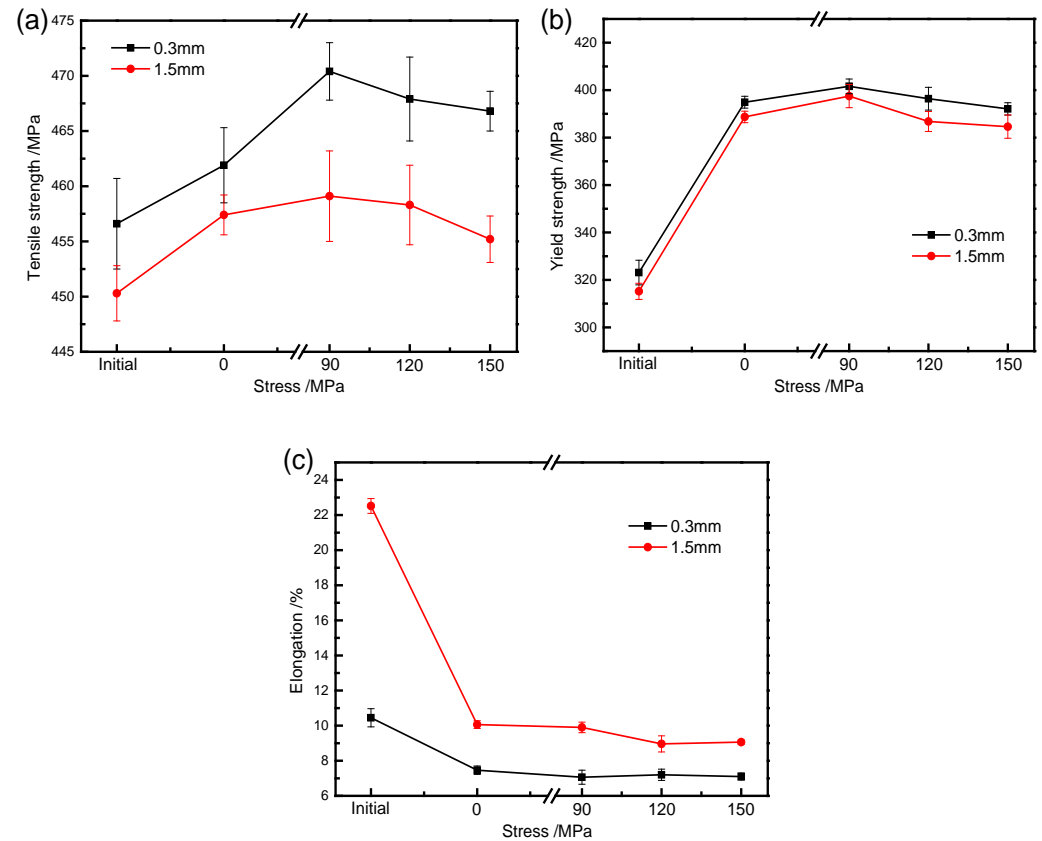


Figure 5. The mechanical properties of initial state AA2024 and AA2024 aged at 453 K under various stresses: (a) tensile strength; (b) yield strength; and (c) elongation.

As a complement to the mechanical analysis, an SEM analysis was performed to obtain more information on the tensile fracture morphology of specimens with different thicknesses. As shown in Figure 6, it can be seen that the fracture mechanism exhibited a typical ductile fracture mode, and there were many second phase particles in some large and deep dimples, and a large number of relatively small dimples were attached. There were also tear ridges extending in different directions on the surface of these dimples, which were intertwined and interconnected, showing that the specimen underwent a large amount of deformation before fracture. Compared with the initial state fracture morphology, the dimples of 0.3 mm specimens were shallower and fewer than those of the 1.5 mm specimens, with a few quasi-cleavage fractures at the edges, which showed quasi-cleavage and toughness fractures, while the 1.5 mm specimens showed dimple fractures. After the creep age process, intergranular fractures occurred in both specimens, and the dimple size and depth decreased, implying that a lower plastic strain was retained, which explains why the elongation decreased greatly. According to previous studies, the changes of precipitates and dislocations after creep age also had great influences on tensile fractures, and a TEM test was carried out.

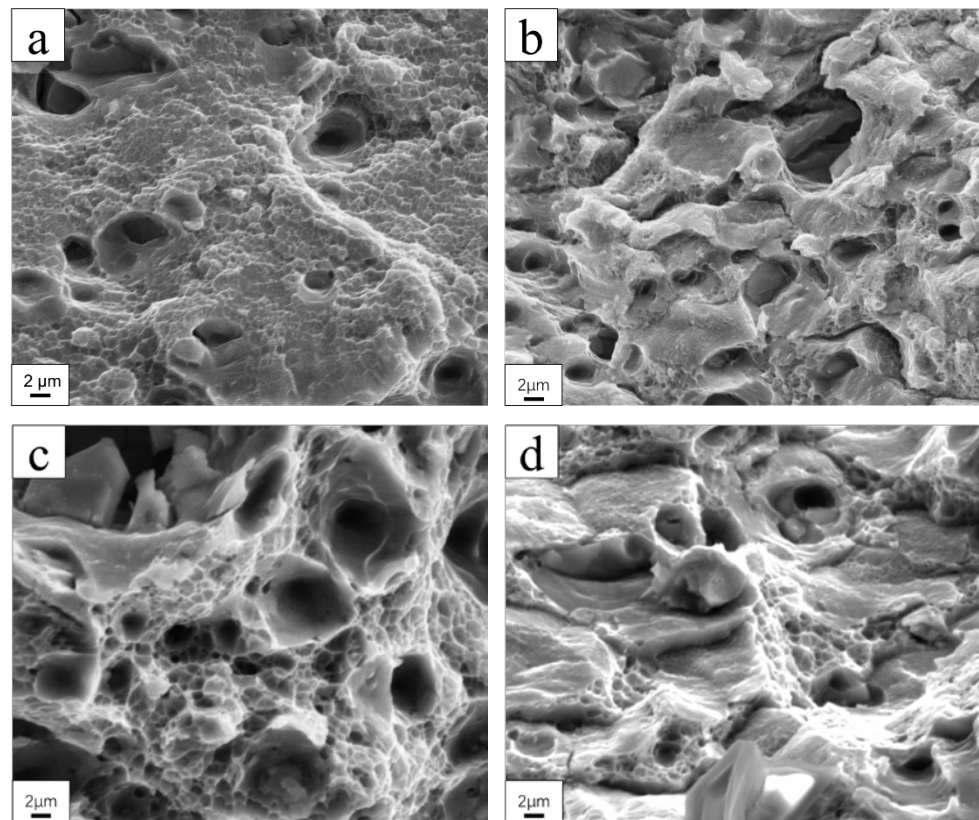


Figure 6. SEM images of fracture surface of tensile specimens under different conditions: (a) 0.3 mm, initial state; (b) 0.3 mm, 12 h aging at 453 K with stress of 90 MPa; (c) 1.5 mm, initial state; (d) 1.5 mm, 12 h aging at 453 K with stress of 90 MPa.

3.3. Microstructure Evolution

According to previous research on AA2024 aluminum alloy [29], the precipitation sequence is as follows: $SSS \rightarrow \text{Guinier-Preston-Bagaryatsky (GPB)} \rightarrow S'' \rightarrow S$. As displayed clearly in Figure 7a,c, there was no diffraction spot in the diffraction pattern, which means that there was no precipitate in the grains, except some dispersed T ($\text{Al}_{20}\text{Cu}_2\text{Mn}_3$) phases. Researchers [30] have shown that these T-phase particles are formed during the homogenization treatment of the alloy and are very stable during the subsequent processing, so there is no significant change during the aging treatment. As seen in Figure 7b,d, with the incident beam along the $[001]_{\text{Al}}$ zone axis, these S phases were $[010]_s$ and $[001]_s$ lath variants [31,32]. After 12 h of aging without stress, the specimens with different thicknesses showed lath-like S phases dispersing in the grains, with continuous second phase particles appearing on the grain boundaries. The microstructure changes of different specimens with increases of stress levels are shown in Figure 8. The electron beams of TEM bright field images were also close to $[100]_{\text{Al}}$. When the stress level was 90 MPa, the size of S phases became smaller, and the number of precipitates increased more than those without stress. It should be noted that there was a small amount of θ phases in the grains, in addition to S phases. In the precipitation process of AA2024 aluminum alloy, there is a competitive relationship between the S phase and the θ phase, and the external stress presents a greater impact on the θ phase than the S phase [33]. When the stress level was increased to 120 MPa, it can be seen that the precipitates showed little change, while the dislocation density obviously increased. However, with the stress increasing to 150 MPa, the precipitates grew up in both length and width, which means the precipitates began to coarsen in size and decrease in number.

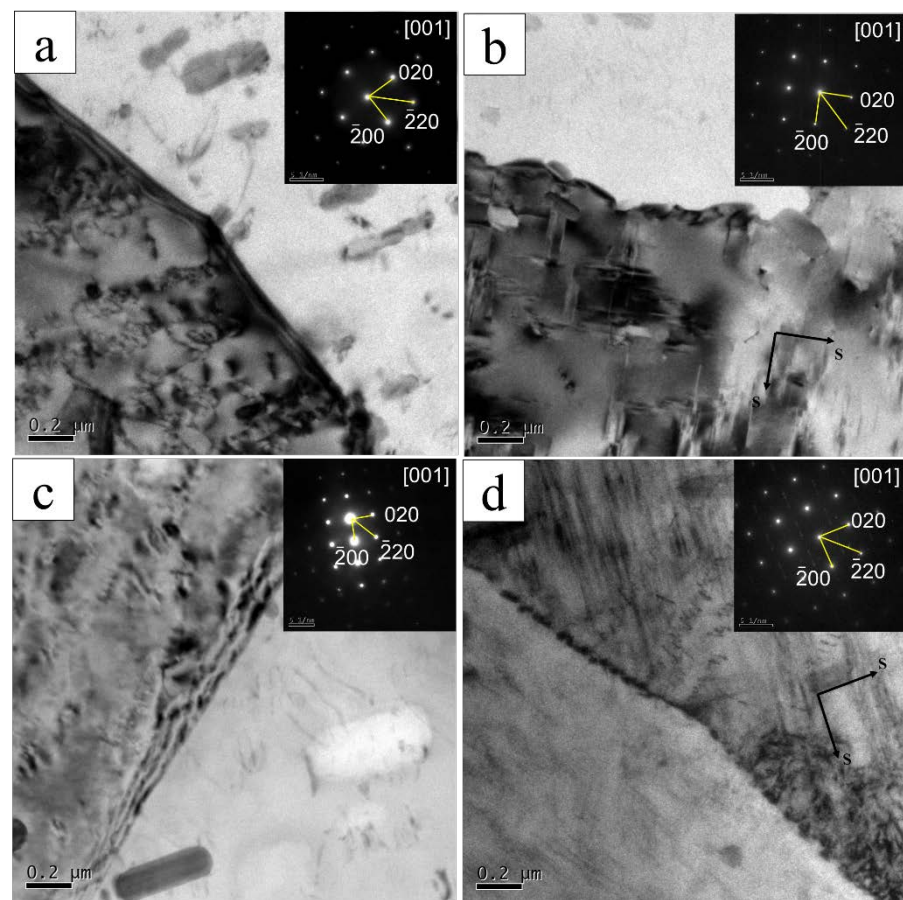


Figure 7. TEM micrographs and corresponding selected area electron diffraction patterns of AA2024 alloy: (a) 0.3 mm, initial state; (b) 0.3 mm, 12 h aging at 453 K without stress; (c) 1.5 mm, initial state; (d) 1.5 mm, 12 h aging at 453 K without stress.

The evolution of the length of S phases shown in Figure 9 was statistically analyzed to investigate the effect of stress levels produced by the manufacturing process. With the increase of stress, the precipitates first became fine and dispersed and then grew up and coarsened. Creep age of AA2024 aluminum alloy is essentially a process of enrichment and change of solute atoms in the alloy. The nucleation and growth of the S phase in the GPB region are the result of short-range ordering of Cu and Mg atoms in the Al matrix. With the increase of stress, the dislocation and stacking fault of α -AL are the preferred nucleation sites in the GPB region, which accelerates the nucleation rate of GPB [34]. Therefore, the S phases aging with stress were more numerous and smaller than those without stress. Moreover, the dislocations were densely dispersed in the grain, which not only facilitated the formation of the GPB region but also enhanced the strength of the AA2024 aluminum alloy. However, the interaction mechanism between dislocations and precipitates changes with the size of precipitates [35]. When the precipitates are small, the dislocations can cut through them; as the size increases, the mechanism changes from a cutting mechanism to a bypass mechanism. Finally, the precipitates interacted with dislocations, hindering dislocation motion and causing alloy strengthening. In addition, the grain boundary and sub-grain boundary were the areas with dense defects conducive to the formation of precipitates, and then it was difficult for precipitates to form near the grain boundary due to the vacancy concentration gradient and the lack of solute atoms, and thus the precipitation-free zone forming around the grain boundary. Therefore, the yield strength and tensile strength of AA2024 aluminum alloy increased obviously after creep age. However, with the increase of stress, the precipitates grew up, and the number of precipitates decreased. As a

result, the mechanical properties of AA2024 aluminum alloy decreased, and the fracture mode also changed, which is consistent with the fracture morphology analysis.

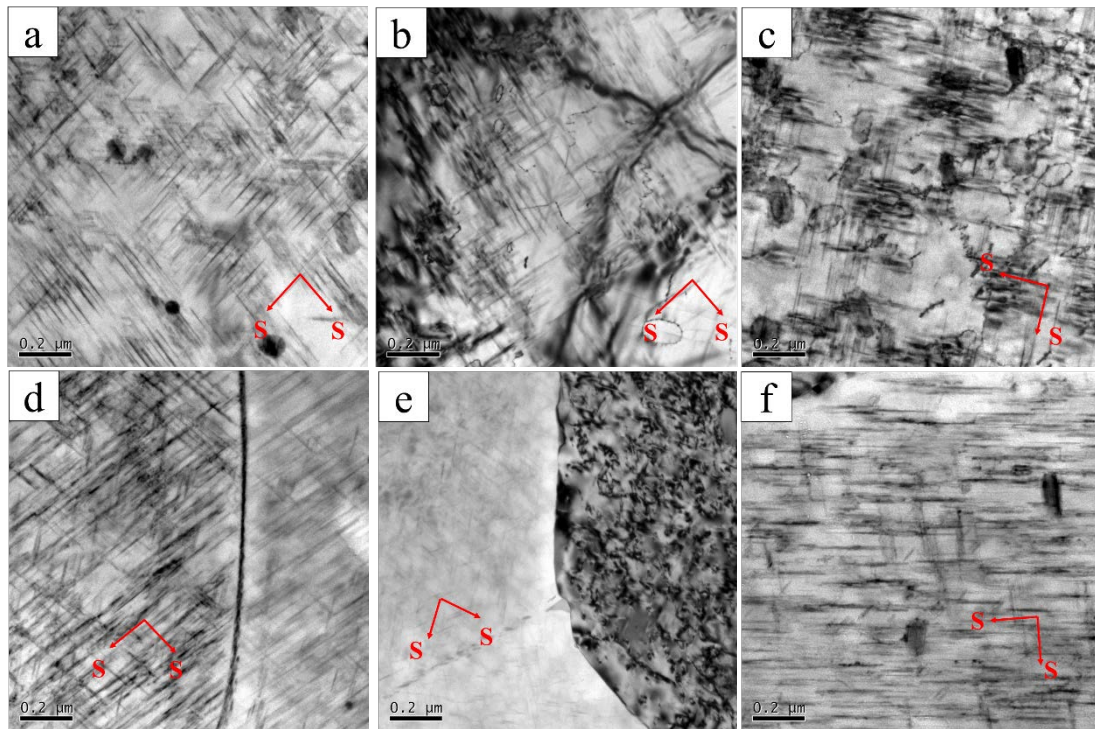


Figure 8. TEM bright field (BF) images of AA2024 alloy under different conditions, where the electron beam was close to $[001]_{Al}$: (a) 0.3 mm, 90 MPa; (b) 0.3 mm, 120 MPa; (c) 0.3 mm, 150 MPa; (d) 1.5 mm, 90 MPa; (e) 1.5 mm, 120 MPa; (f) 1.5 mm, 150 MPa.

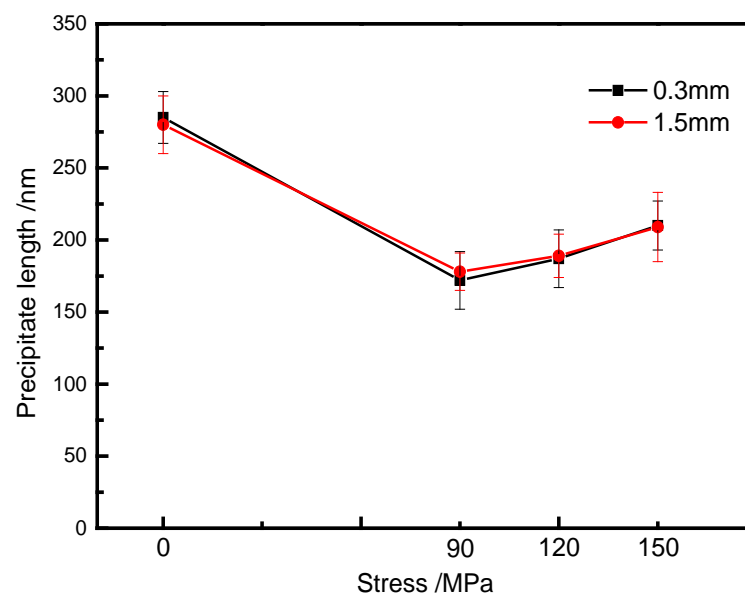


Figure 9. The precipitates length of AA2024 after different creep ages.

3.4. Discussion

The main factors affecting creep deformation of alloys can be summarized as follows [36]: (i) dislocation climb-glide, which includes the dislocation climbing to a parallel slip or gliding on the new plane by thermal activation; (ii) dislocation creep, which means the dislocation passing the obstacle and getting into a lower energy state by vacancy diffusion; and (iii) grain boundary slide, which occurs by the movement of dislocations along the boundary by a

combination of climb and glide. Based on the macroscopic properties, the creep strains of different thicknesses of specimens were basically the same, and the initial state of them was also same. From the microstructure, the morphology and size of precipitates were similar, and their dislocation movement mechanism was the same under this process condition. In conclusion, the thickness has no effect on the creep behavior at this scale.

4. Non-Isothermal Creep Constitutive and Numerical Modeling

4.1. The Non-Isothermal Creep Behavior of AA2024 Aluminum Alloy

The deformations of 0.3 mm thick specimens under different stress levels during forming are shown in Figure 10, where the without stress original curve is used to describe the thermal behavior of AA2024 aluminum alloy. In the heating stage and holding stage, the deformation increased and then began to decrease in the cooling stage. With the increase of stress levels, the deformation improved. Tahami [37] divided the deformation of alloys during creep into elastic deformation, plastic deformation, and creep deformation. In this study, the applied stress was far less than the yield strength of AA2024 aluminum alloys, so the plastic deformation could be assumed to be zero. Moreover, in our previous study [38], the change in elastic modulus of aluminum alloy was small, which could also be assumed to be irrelevant and ignored. Therefore, the deformation of AA2024 aluminum alloy can be summarized as elastic deformation ($\varepsilon_{\text{elastic}}$), creep deformation ($\varepsilon_{\text{creep}}$), and thermal deformation ($\varepsilon_{\text{thermal}}$), and the expression is as follows:

$$\varepsilon_{\text{alloy}} = \varepsilon_{\text{elastic}} + \varepsilon_{\text{creep}} + \varepsilon_{\text{thermal}} \quad (1)$$

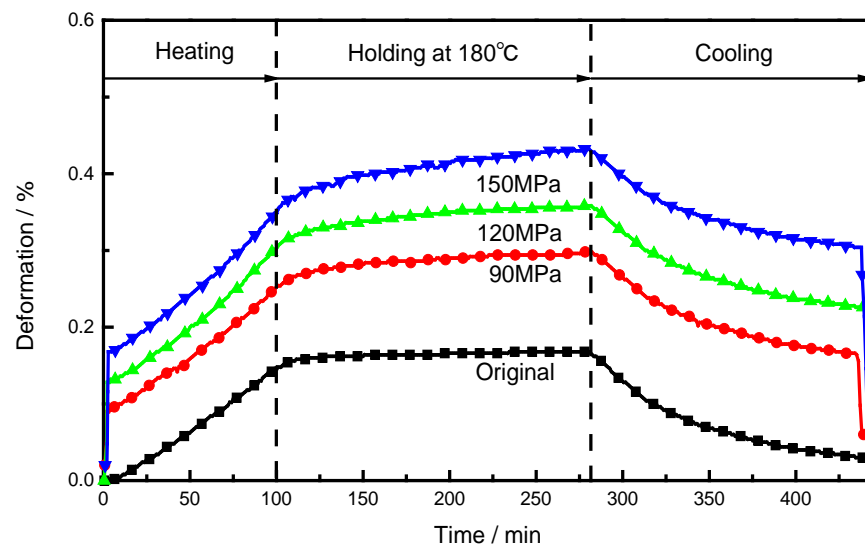


Figure 10. The deformation curves of the AA2024 aluminum alloy during non-isothermal loading.

The creep strain can be obtained by Equation (1) (see Figure 11). Generally, the creep behavior of most aluminum alloys can be divided into the primary creep stage, steady-state creep stage, and accelerated creep stage [39]. However, in the FML-forming process, the creep behavior of AA2024 aluminum alloy includes six stages [38]. Specifically, there is an initial zero creep stage (stage I) and a heating accelerated creep stage (stage II) during the heating process. After that, a typical primary creep stage (stage III) and a steady-state creep stage (stage IV) occur during the holding process. Then in the cooling process, a cooling decelerated creep stage (stage V) appears, ending with a second zero creep stage (stage VI). The creep behavior suggests that the effect of the stress level is significant. With the increase of applied stress, the creep strain increases obviously, and the durations of stage I and stage VI decrease. This is because the high stress increases the movement of dislocations, which promotes creep.

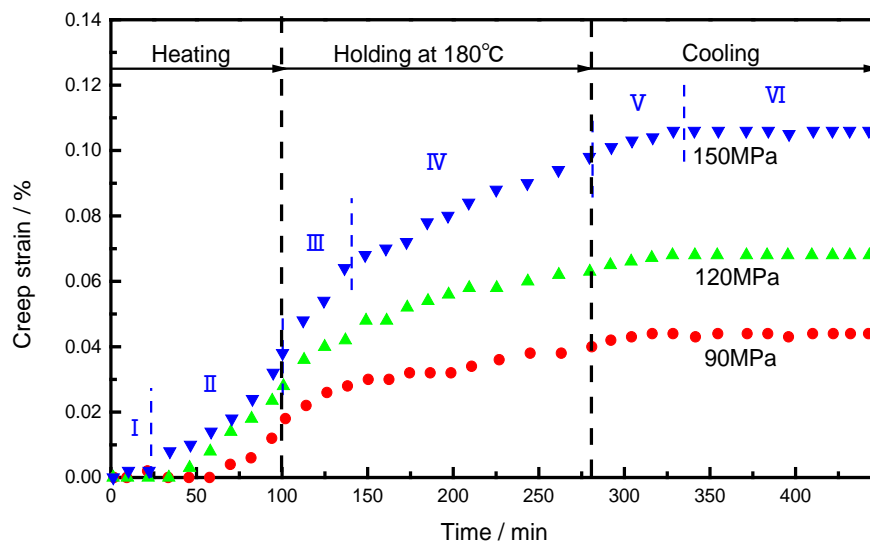


Figure 11. The creep deformation behaviors of the AA2024 aluminum alloy with various stresses during non-isothermal process.

To further demonstrate the difference between the non-isothermal process and the isothermal process, the comparison results of creep strain are presented in Table 1. It can be seen that the creep strain of the non-isothermal process is larger than that of the isothermal process under the same applied stress condition. Moreover, the creep strain of non-isothermal and isothermal processes both improve with the increase of applied stress. In the non-isothermal process, the creep strain in the holding process is the largest among the three stages, and the creep strain in the heating process is also considerable. The creep strain in the heating process and the holding process accounts for more than 90% of the total creep strain. The results indicate that there are some differences between non-isothermal and isothermal processes, which need to be paid attention to for the modeling.

Table 1. The isothermal and non-isothermal creep strains of the AA2024 aluminum alloy.

	Stress/MPa	Creep Strain (%), Percentage of Total Creep Strain				Increment
		Heating	Holding	Cooling	Total	
Isothermal	90 MPa	0, 0	0.034, 100%	0, 0	0.034	-
	120 MPa	0, 0	0.056, 100%	0, 0	0.056	-
	150 MPa	0, 0	0.072, 100%	0, 0	0.072	-
Non-isothermal	90 MPa	0.018, 40.9%	0.022, 50.0%	0.004, 9.1%	0.044	29.4%
	120 MPa	0.028, 41.2%	0.035, 51.5%	0.005, 7.3%	0.068	21.4%
	150 MPa	0.038, 35.8%	0.06, 56.6%	0.008, 7.6%	0.106	47.2%

4.2. Constitutive Modeling

In this study, unified creep damage constitutive modeling of aluminum alloys based on the unified theory and aging dynamics was used [40,41]. This modeling combined the stress–strain relationship of material with microstructural evolution, such as second phase precipitation and grain growth. It could describe the creep behavior and physical mechanisms, which has considerable scientific significance and engineering guidance value.

The unified constitutive creep should focus on the early stages of creep behavior, which is governed by relatively low stress and complicated temperature variation [42].

In order to facilitate the description, modified modeling, which considers the effect of temperature change on the creep strain rate, is shown as follows:

$$\dot{\varepsilon} = \begin{cases} 0 & , \sigma < \sigma_0 \\ A \cdot \sinh [B \cdot (\sigma - \sigma_0) (1 - H)^{m_0}] \cdot \exp\left(-\frac{Q_c}{RT}\right) & , \sigma > \sigma_0 \end{cases} \quad (2)$$

$$\dot{H} = \frac{h}{\sigma^{m_1}} \cdot \left(1 - \frac{H}{H^*}\right) \cdot \exp\left(\frac{Q_H}{RT}\right) \cdot \dot{\varepsilon} \quad (3)$$

$$\sigma_0 = C_1 \cdot \exp\left(\frac{C_2}{T_v}\right) \quad (4)$$

where A , B , h , H^* , m_0 , and m_1 are material constants; T_v means current temperature (K); Q_c represents the creep apparent activation energy; Q_H represents the hardening apparent activation energy; R is the gas molar constant; and T is the creep age temperature (K).

In Equation (2), σ_0 describes the threshold stress, which decreases with increasing temperature. The σ_0 expression (Equation (4)) can be fitted according to the previous experimental results, as shown in Figure 12. The beginning of creep can be controlled and judged by Equation (4). In Equation (3), variable H describes the primary creep stage, which varies from 0 at the beginning of the creep process to H^* . H^* ($0 < H^* < 1$) reflects the work-hardening influence and controls the creep strain rate, and H^* , which limits the dislocation strengthening, is the saturation value of H . The parameters A and B characterize the steady-state creep stage. To obtain accurate constants, an intelligent algorithm, namely, particle swarm optimization (PSO), was employed [43], and the material constants are listed in Table 2. In conclusion, a unified creep constitutive model, which can describe the creep behavior of AA2024 aluminum alloy under non-isothermal conditions and stress levels, was established.

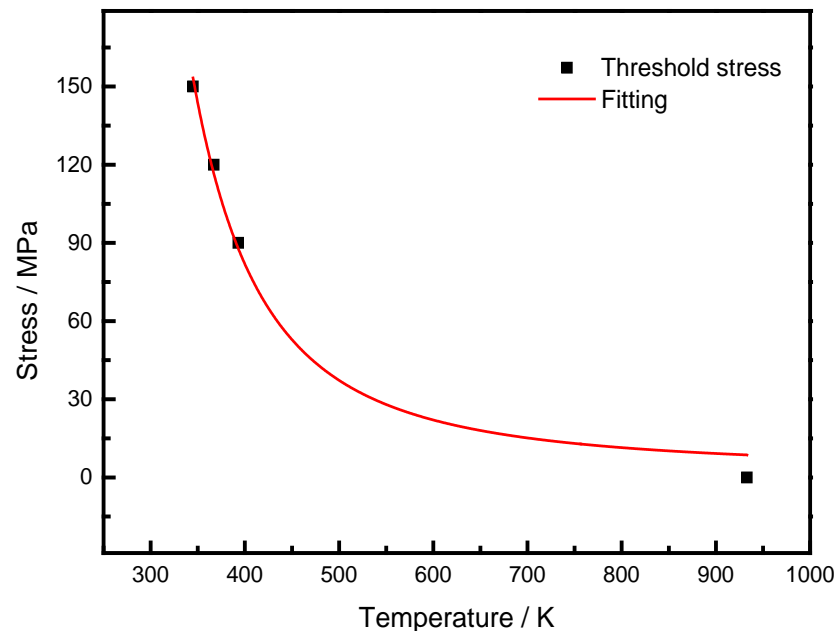


Figure 12. The threshold stresses and fitting curve.

4.3. Finite Elements Simulation Modeling

In order to verify the validity of the established creep age constitutive model in the FE solver ABAQUS, an FE model of the non-isothermal tensile creep test at 453 K for AA2024 aluminum alloy was made. Reduced integration 8-node linear elements (C3D8R) were used in the FE model, which are suitable for both thin and thick solids (see Figure 13a). The sizes of grids were all 2 mm, and the number of elements was 887. A Young's modulus of 71 GPa

and Poisson's ratio of 0.33 were assigned to the studied AA2024 aluminum alloy [44]. The constitutive model of the aluminum sheet, described in Section 4.2, was programmed by the FORTRAN language and implemented into ABAQUS via the user-defined subroutine CREEP. Moreover, the gradients $\partial\Delta p/\partial p$ and $\partial\Delta p/\partial\sigma_e$ were precisely determined, and the step time could be controlled effectively by the implicit integration of ABAQUS. The experimental results and calculated results were compared to verify the above model, as shown in Figure 13b. The experimental data and fitting results were clearly in good agreement. In addition, the creep strain values under other conditions were calculated by using the constitutive model, as shown in Figure 13c. The maximum error between the calculated and measured values was about 9%, which indicates that the constitutive model has a good ability to describe each creep stage of AA2024 aluminum alloy during the non-isothermal process in FE solver.

Table 2. Creep-constitutive parameters for AA2024 aluminum alloy.

Parameter	Symbol	Value	Unit
Creep constant for steady-state stage	A	2.59×10^8	h^{-1}
Creep constant for steady-state stage	B	0.375	MPa^{-1}
Creep constant for primary stage	h	2.335	MPa
Creep constant for primary stage	H^*	0.917	-
Stress-dependent hardening index	m_0	0.904	-
Stress sensitivity coefficient	m_1	0.508	-
Creep apparent activation energy	Q_c	110.2	$\text{kJ}\cdot\text{mol}^{-1}$
Hardening apparent activation energy	Q_H	19.98	$\text{kJ}\cdot\text{mol}^{-1}$
Stress-temperature coefficient	C_1	1.6	MPa
Stress-temperature coefficient	C_2	1574	K

4.4. Discussion

To explain the creep behavior of AA2024 aluminum alloy during non-isothermal processes, the relationship between threshold stress and temperature was introduced. Usually, the creep behavior in the hyperbolic sine equation is controlled by the coefficient of dislocation substructure and precipitates [45]. During the heating process, the high level stress providing higher level initial dislocations enhance dislocation movement, which can accelerate the creep process and reduce the creep resistance. Hence, a lower temperature is expected when creep occurs with higher stress levels. In addition, it is known that creep deformation is a thermally activated time-dependent process with assisting stress [46]. Therefore, the relationship between temperature and stress can be converted into the relationship between apparent activation energy and stress, which can be expressed by the difference between the thermal activation energy and the stress-assisted energy [47,48].

$$Q_c = Q_0 - (\sigma - \sigma_0) \times V \quad (5)$$

where Q_0 is the thermal activation energy, and V is the activation volume. $\sigma \times (\sigma - \sigma_0)$ is the temperature-dependent component (effective stress). It is observed that the effective stress is decreased with temperature and tends to be zero. Moreover, during the creep process, the activation volume and the internal stress are considered to be independent at a fixed temperature and total strain range [49], and previous work on single crystals also shows that the activation energy Q_c for creep should be a function of temperature [50]. Then the relationships between threshold stress and temperature can be evaluated by the Arrhenius equation.

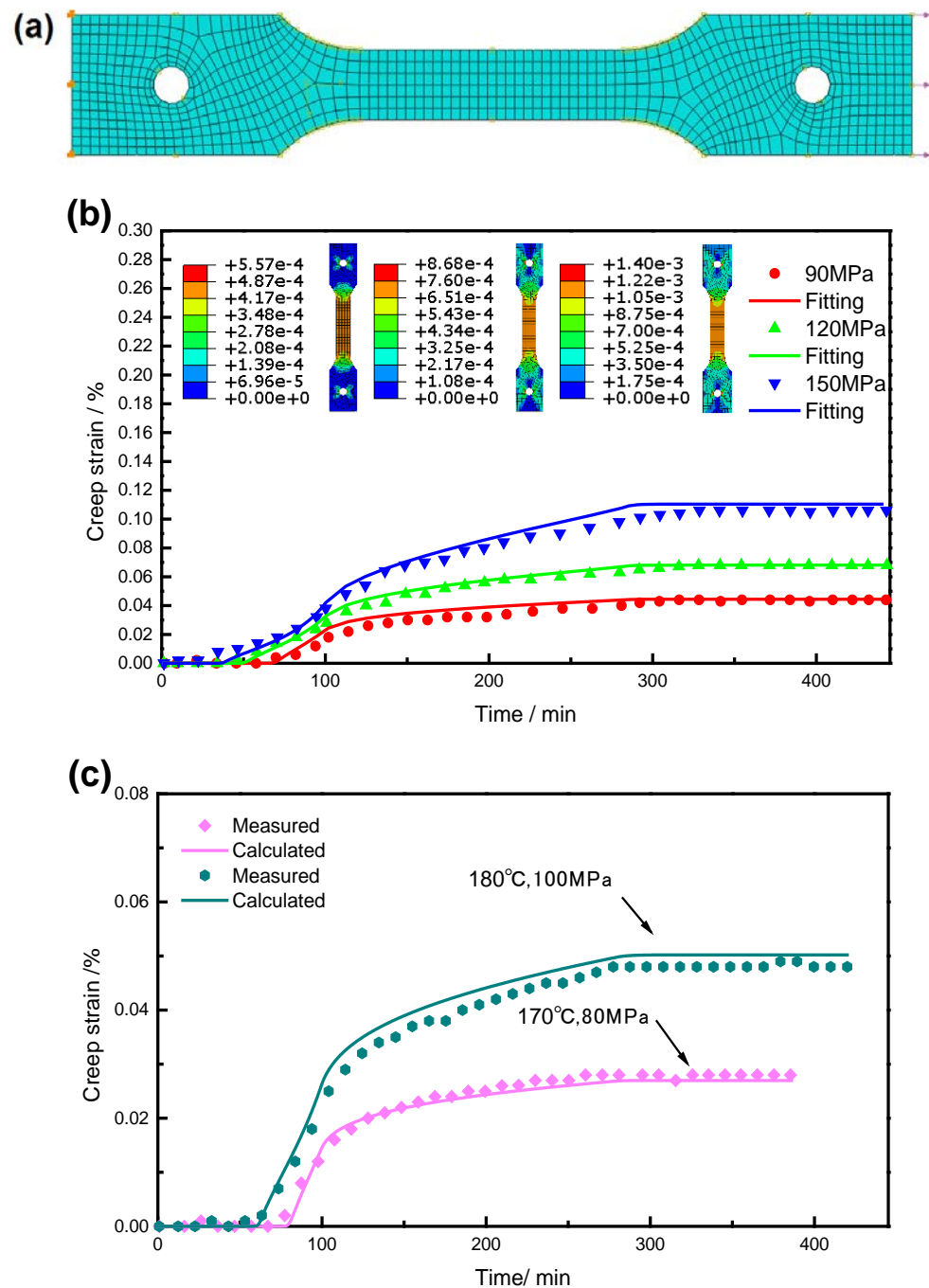


Figure 13. Comparisons between experimental and calculated results of creep tests: (a) FE mesh used in the present work; (b) fitting creep strain; (c) calculated creep strain.

In general, the creep mechanism can be determined by the theoretically predicted values of stress exponent n and apparent activation energy Q_c [51]. For AA2024 aluminum alloy, stress exponents of $n = 2\text{--}5$ indicate that dislocation glide or dislocation climb is dominant in terms of creep mechanism [52–54]. The apparent activation energy Q_c , which fits by constitutive modeling, is approximately 105 kJ/mol during the non-isothermal process. Lin [54] reported that the average apparent activation of AA2024 aluminum alloy is 85 kJ/mol under 185–225 MPa at 423–473 K. Obviously, the calculated apparent activation energy is higher than in previous reports but is lower than that for self-diffusion energy in pure aluminum (142 kJ/mol) [55]. This is due to the thermodynamic mechanism of dislocation movement. Creep in aluminum alloys mainly occurs as a result of dislocation

slipping. Dislocations cannot move randomly when the energy barrier is increased by the reduced applied stress [56]. Moreover, during the heating process, dislocation movement cannot overcome the energy barrier at low temperatures. Feng et al. also proved that the activation energy increases with reduction of temperature [57]. Therefore, the creep behavior of AA2024 aluminum alloy is mainly controlled by the dislocation glide mechanism during the non-isothermal process. To further analyze the sensitivity of apparent activation energy Q_c , the creep strain under 120 MPa was compared, as shown in Figure 14. When the apparent activation energy Q_c increases or decreases, the creep occurs at different time, and the creep strains at different Q_c stages are also quite distinct, which illustrates the importance of establishing constitutive modeling to analyze the springback deformation of FMLs during the non-isothermal process.

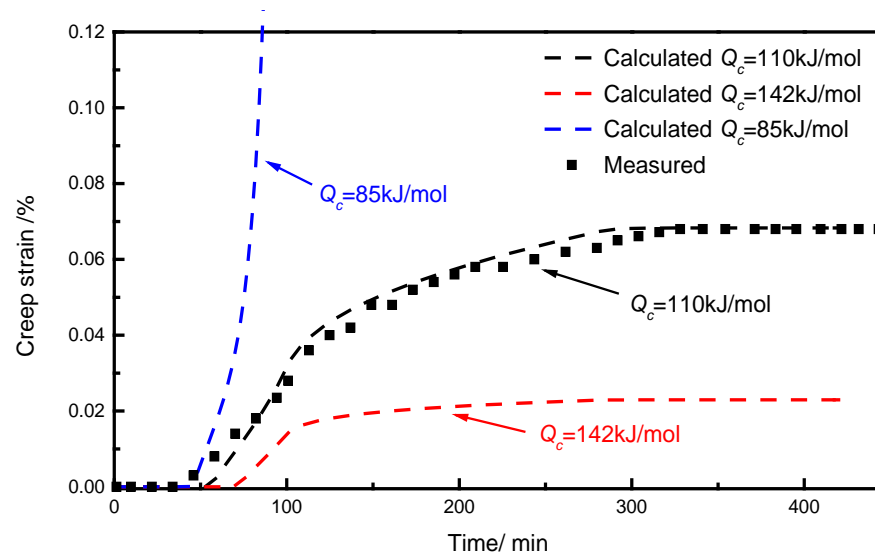


Figure 14. Sensitivity analysis of apparent activation energy Q_c on creep strain.

5. Conclusions

In this study, the effects of specimen thickness and the non-isothermal process on the creep behavior of AA2024 aluminum alloy were determined based on creep strains, mechanical properties, and microstructure results. Then, constitutive modeling used for the non-isothermal process was proposed. The main contributions and findings of the present study can be summarized as follows:

(1) Comparing the creep behavior between specimens of different thicknesses, the variation of creep strain is no more than 5.35%. The size and morphology of precipitates of specimens of different thicknesses are close to each other. Only the mechanical properties are affected by initial specimen thickness, with a difference about 10 MPa. It can be concluded that the thickness has little effect on the creep behavior of specimens at the present scale.

(2) The S phase and θ phase are observed in AA2024 aluminum alloy, and stress promotes finer precipitates for the S phase for the θ phase. With the increase of stress level, the precipitates first become fine and dispersed and then grow up and coarsen. Mechanical properties change with the morphology of precipitates. Therefore, controlling the process to strengthen the alloy properties is crucial during FML manufacturing.

(3) Creep behavior of AA2024 aluminum alloy under the non-isothermal process of FMLs was investigated. The non-isothermal creep behavior with six stages is quite different than the isothermal creep behavior. Creep strain in the heating stage and holding stage of the non-isothermal process is more than 90% of the total creep strain. The results show that the creep strain of the heating stage cannot be ignored in the manufacturing process of FMLs.

(4) The differences between the isothermal process and the non-isothermal process were discussed, and a creep constitutive model for AA2024 aluminum alloy that can reflect

the creep behavior in the non-isothermal process was established. The calculated results agree well with the experimental data, which is helpful to further analyze deformation.

Author Contributions: Writing—original draft, investigation and resources, X.W.; Funding acquisition and project administration, L.Z.; Methodology and validation, Y.Y.; Conceptualization and formal analysis, Y.X.; Data curation, software and visualization, Q.Z.; Writing—review & editing and formal analysis, X.Y. All authors have read and agreed to the published version of the manuscript.

Funding: This research was funded by the Open Research Fund of State Key Laboratory of High Performance Complex Manufacturing, Central South University (Kfkt2021-02), the National Natural Science Foundation of China (No. 51675538) and the Science Foundation for Young Scientists of Lanzhou Jiaotong University (No. 2020042).

Data Availability Statement: Not applicable.

Conflicts of Interest: The authors declare no conflict of interest.

References

1. Jata, K.V. *Lightweight Alloys for Aerospace Applications*; John Wiley & Sons: Hoboken, NJ, USA, 2001.
2. Hirschab, J. Superior light metals by texture engineering: Optimized aluminum and magnesium alloys for automotive applications. *Acta Mater.* **2013**, *61*, 818–843. [[CrossRef](#)]
3. Vermeeren, C.A.J.R. An Historic Overview of the Development of Fibre Metal Laminates. *Appl. Compos. Mater.* **2003**, *10*, 189–205. [[CrossRef](#)]
4. Chai, G.B.; Manikandan, P. Low velocity impact response of fibre-metal laminates—A review. *Compos. Struct.* **2014**, *107*, 363–381. [[CrossRef](#)]
5. Zarei, H.; Fallah, M.; Minak, G.; Bisadi, H.; Daneshmehr, A.R. Low velocity impact analysis of Fiber Metal Laminates (FMLs) in thermal environments with various boundary conditions. *Compos. Struct.* **2016**, *149*, 170–183. [[CrossRef](#)]
6. Bieniaś, J.; Dadej, K.; Surowska, B. Interlaminar fracture toughness of glass and carbon reinforced multidirectional fiber metal laminates. *Eng. Fract. Mech.* **2017**, *175*, 127–145. [[CrossRef](#)]
7. Safari, M.; Salamat-Talab, M.; Abdollahzade, A.; Akhavan-Safar, A.; da Silva, L.F.M. Experimental investigation, statistical modeling and multi-objective optimization of creep age forming of fiber metal laminates. *Proc. Inst. Mech. Eng. Part L* **2020**, *234*, 1389–1398. [[CrossRef](#)]
8. Zafar, R.; Lang, L.; Zhang, R. Experimental and numerical evaluation of multilayer sheet forming process parameters for light weight structures using innovative methodology. *Int. J. Mater. Form.* **2016**, *9*, 35–47. [[CrossRef](#)]
9. Vermeeren, C.A.J.R.; Beumler, T.; De Kanter, J.L.C.G.; Van Der Jagt, O.C.; Out, B.C.L. Glare Design Aspects and Philosophies. *Appl. Compos. Mater.* **2003**, *10*, 257–276. [[CrossRef](#)]
10. Soutis, C. Fibre reinforced composites in aircraft construction. *Prog. Aerosp. Sci.* **2005**, *41*, 143–151. [[CrossRef](#)]
11. Zhu, A.W.; Starke, E.A. Stress aging of Al-xCu alloys: Experiments. *Acta Mater.* **2001**, *49*, 2285–2295. [[CrossRef](#)]
12. Safari, M.; De Sousa, R.A.; Fernandes, F.; Salamat-Talab, M.; Abdollahzadeh, A. Creep Age Forming of Fiber Metal Laminates: Effects of Process Time and Temperature and Stacking Sequence of Core Material. *Materials* **2021**, *14*, 7881. [[CrossRef](#)]
13. Li, Y.; Rong, Q.; Shi, Z.; Sun, X.; Meng, L.; Lin, J. An accelerated springback compensation method for creep age forming. *Int. J. Adv. Manuf. Technol.* **2019**, *102*, 121–134. [[CrossRef](#)]
14. Bažant, Z.P.; Hauggaard, A.B.; Baweja, S.; Ulm, F.J. Microprestress-Solidification Theory for Concrete Creep. I: Aging and Drying Effects. *J. Eng. Mech.* **1997**, *123*, 1188–1194. [[CrossRef](#)]
15. Zhan, L.; Lin, J.; Dean, T.A. A review of the development of creep age forming: Experimentation, modelling and applications. *Int. J. Mach. Tools Manuf.* **2011**, *51*, 1–17. [[CrossRef](#)]
16. Arabi, R.; Zohdi, H.; Shahverdi, H.R.; Bozorg, M.; Hadavi, S.M.M. Influence of multi-step heat treatments in creep age forming of 7075 aluminum alloy: Optimization for springback, strength and exfoliation corrosion. *Mater. Charact.* **2012**, *73*, 8–15. [[CrossRef](#)]
17. Zhan, L.; Li, W.; Ma, Q.; Liu, L. The Influence of Different External Fields on Aging Kinetics of 2219 Aluminum Alloy. *Metals* **2016**, *6*, 201. [[CrossRef](#)]
18. Yang, Y.; Zhan, L.; Shen, R.; Yin, X.; Li, X.; Li, W.; Huang, M.; He, D. Effect of pre-deformation on creep age forming of 2219 aluminum alloy: Experimental and constitutive modelling. *Mater. Sci. Eng. A* **2017**, *683*, 227–235. [[CrossRef](#)]
19. Gonzalez-Canche, N.G.; Flores-Johnson, E.A.; Carrillo, J.G. Mechanical characterization of fiber metal laminate based on aramid fiber reinforced polypropylene. *Compos. Struct.* **2017**, *172*, 259–266. [[CrossRef](#)]
20. Floreen, S. The creep fracture characteristics of nickel-base superalloy sheet samples. *Eng. Fract. Mech.* **1979**, *11*, 55–60. [[CrossRef](#)]
21. Mills, W.J.; Hertzberg, R.W. The effect of sheet thickness on fatigue crack retardation in 2024-T3 aluminum alloy. *Eng. Fract. Mech.* **1975**, *7*, 705–711. [[CrossRef](#)]
22. Mahmoud, S.; Lease, K. The effect of specimen thickness on the experimental characterization of critical crack-tip-opening angle in 2024-T351 aluminum alloy. *Eng. Fract. Mech.* **2003**, *70*, 443–456. [[CrossRef](#)]

23. Lebert, A.A.; Besson, J.; Gourgues, A.F. Fracture of 6056 aluminum sheet materials: Effect of specimen thickness and hardening behavior on strain localization and toughness. *Mater. Sci. Eng. A* **2005**, *395*, 186–194. [[CrossRef](#)]
24. Pindera, M.J.; Williams, T.O.; Macheret, Y. Time-dependent response of aramid-epoxy-aluminum sheet, ARALL, laminates. *Polym. Compos.* **1989**, *10*, 328–336. [[CrossRef](#)]
25. Daghighi, V.; Khalili, S.M.R.; Eslami Farsani, R. Creep behavior of basalt fiber-metal laminate composites. *Compos. Part B Eng.* **2016**, *91*, 275–282. [[CrossRef](#)]
26. Abouhamzeh, M.; Sinke, J.; Benedictus, R. A large displacement orthotropic viscoelastic model for manufacturing-induced distortions in Fibre Metal Laminates. *Compos. Struct.* **2019**, *209*, 1035–1041. [[CrossRef](#)]
27. Zhan, L.; Wu, X.; Wang, X.; Yang, Y.; Liu, G.; Xu, Y. Effect of Process Parameters on Fatigue and Fracture Behavior of Al-Cu-Mg Alloy after Creep Aging. *Metals* **2018**, *8*, 298. [[CrossRef](#)]
28. Wu, X.; Zhan, L.; Zhao, X.; Wang, X.; Chang, T. Effects of surface pre-treatment and adhesive quantity on interface characteristics of fiber metal laminates. *Compos. Interfaces* **2020**, *27*, 829–843. [[CrossRef](#)]
29. Radmilovic, V.; Kilaas, R.; Dahmen, U.; Shiflet, G.J. Structure and morphology of S-phase precipitates in aluminum. *Acta Mater.* **1999**, *47*, 3987–3997. [[CrossRef](#)]
30. Xu, Y.; Zhan, L.; Xu, L.; Huang, M. Experimental research on creep aging behavior of Al-Cu-Mg alloy with tensile and compressive stresses. *Mater. Sci. Eng. A* **2017**, *682*, 54–62. [[CrossRef](#)]
31. Fu, R.; Xu, H.; Luan, G.; Dong, C.; Zhang, F.; Li, G. Top surface microstructure of friction-stir welded aa2524-t3 aluminum alloy joints. *Mater. Charact.* **2012**, *65*, 48–54. [[CrossRef](#)]
32. Dan, W.J.; Zhang, W.G.; Li, S.H.; Lin, Z.Q. An experimental investigation of large-strain tensile behavior of a metal sheet. *Mater. Des.* **2007**, *28*, 2190–2196. [[CrossRef](#)]
33. Zhang, F.; Levine, L.E.; Allen, A.J.; Campbell, C.E.; Creuziger, A.A.; Kazantseva, N.; Ilavsky, J. In situ structural characterization of ageing kinetics in aluminum alloy 2024 across angstrom-to-micrometer length scales. *Acta Mater.* **2016**, *111*, 385–398. [[CrossRef](#)] [[PubMed](#)]
34. Charai, A.; Walther, T.; Alfonso, C.; Zahra, A.M.; Zahar, C.Y. Coexistence of clusters, GPB zones, S''-, S'- and S-phases in an Al-0.9% Cu-1.4% Mg alloy. *Acta Mater.* **2000**, *48*, 2751–2764. [[CrossRef](#)]
35. Singh, C.V.; Warner, D.H. Mechanisms of Guinier–Preston zone hardening in the athermal limit. *Acta Mater.* **2010**, *58*, 5797–5805. [[CrossRef](#)]
36. Li, D.F.; O Dowd, N.P.; Davies, C.M.; Nikbin, K.M. A review of the effect of prior inelastic deformation on high temperature mechanical response of engineering alloys. *Int. J. Press. Vessel. Pip.* **2010**, *87*, 531–542. [[CrossRef](#)]
37. Tahami, F.V.; Daeisorkhabi, A.H.; Biglari, F.R. Creep constitutive equations for cold-drawn 304L stainless steel. *Mater. Sci. Eng. A* **2010**, *527*, 4993–4999. [[CrossRef](#)]
38. Xu, Y.; Zhan, L.; Huang, M.; Shen, R.; Ma, Z.; Xu, L.; Wang, K.; Wang, X. Deformation behavior of Al-Cu-Mg alloy during non-isothermal creep age forming process. *J. Mater. Process. Technol.* **2018**, *255*, 26–34. [[CrossRef](#)]
39. Li, Y.; Shi, Z.; Lin, J.; Yang, Y.L.; Huang, B.M.; Chung, T.F.; Yang, J.R. Experimental investigation of tension and compression creep-ageing behaviour of AA2050 with different initial temps. *Mater. Sci. Eng. A* **2016**, *657*, 299–308. [[CrossRef](#)]
40. Li, Y.; Shi, Z.; Lin, J.; Yang, Y.L.; Balint, D.S. A unified constitutive model for asymmetric tension and compression creep-ageing behaviour of naturally aged Al-Cu-Li alloy. *Int. J. Plast.* **2017**, *89*, 130–149. [[CrossRef](#)]
41. Wang, M.; Zhan, L.; Yang, Y.; Yang, L.; Huang, M. Effect of pre-deformation on aging creep of Al-Li-S4 alloy and its constitutive modeling. *Trans. Nonferrous Met. Soc. China* **2015**, *25*, 1383–1390. [[CrossRef](#)]
42. Kowalewski, Z.L.; Hayhurst, D.R.; Dyson, B.F. Mechanisms-based creep constitutive equations for an aluminium alloy. *J. Strain Anal. Eng. Des.* **1994**, *29*, 309–316. [[CrossRef](#)]
43. Yang, Y.; Zhan, L.; Shen, R.; Liu, J.; Li, X.; Huang, M.; He, D.; Chang, Z.; Ma, Y.; Wan, L. Investigation on the creep-age forming of an integrally-stiffened AA2219 alloy plate: Experiment and modeling. *Int. J. Adv. Manuf. Technol.* **2018**, *95*, 2015–2025. [[CrossRef](#)]
44. Lin, C.T.; Kao, P.W.; Jen, M.H.R. Thermal residual strains in carbon fibre-reinforced aluminium laminates. *Composites* **1994**, *25*, 303–307. [[CrossRef](#)]
45. Khan, A.S.; Liu, J.; Yoon, J.W.; Nambori, R. Strain rate effect of high purity aluminum single crystals: Experiments and simulations. *Int. J. Plast.* **2015**, *67*, 39–52. [[CrossRef](#)]
46. Dorn, J.E. *Creep and Fracture of Metals at High Temperatures*; National Physical Laboratory: Teddington, UK, 1956.
47. Mordike, B.L.; Haasen, P. The influence of temperature and strain rate on the flow stress of α -iron single crystals. *Philos. Mag.* **1962**, *7*, 459–474. [[CrossRef](#)]
48. Conrad, H. *On the Mechanism of Yielding and Flow in Iron*; North American Aviation, Atomics International Division: Canoga Park, CA, USA, 1961.
49. Chang, Y.J.; Nam, S.W.; Ginsztler, J. Activation processes of stress relaxation during hold time in 1Cr–Mo–V steel. *Mater. Sci. Eng. A* **1999**, *264*, 188–193.
50. Montemayor, J.; Gómez Ramírez, R.; Carrillo, E. High-temperature creep on KBr single crystals. *Phys. Status Solidi A* **1976**, *38*, 67–72. [[CrossRef](#)]
51. Zhao, Y.; Fang, Q.; Liu, Y.; Wen, P.; Liu, Y. Creep behavior as dislocation climb over NiAl nanoprecipitates in ferritic alloy: The effects of interface stresses and temperature. *Int. J. Plast.* **2015**, *69*, 89–101. [[CrossRef](#)]

52. Alhamidi, A.; Horita, Z. Grain refinement and high strain rate superplasticity in aluminium 2024 alloy processed by high-pressure torsion. *Mater. Sci. Eng. A* **2015**, *622*, 139–145. [[CrossRef](#)]
53. Malas, J.C.; Venugopal, S.; Seshacharyulu, T. Effect of microstructural complexity on the hot deformation behavior of aluminum alloy 2024. *Mater. Sci. Eng. A* **2004**, *368*, 41–47. [[CrossRef](#)]
54. Lin, Y.C.; Xia, Y.; Chen, M.; Jiang, Y.; Li, L. Modeling the creep behavior of 2024-T3 Al alloy. *Comput. Mater. Sci.* **2013**, *67*, 243–248. [[CrossRef](#)]
55. Sherby, O.D.; Lytton, J.L.; Dorn, J.E. Activation energies for creep of high-purity aluminum. *Acta Metall.* **1957**, *5*, 219–227. [[CrossRef](#)]
56. Shi, C.; Mao, W.; Chen, X.G. Evolution of activation energy during hot deformation of AA7150 aluminum alloy. *Mater. Sci. Eng. A* **2013**, *571*, 83–91. [[CrossRef](#)]
57. Feng, D.; Zhang, X.; Liu, S.; Wu, Z.; Tan, Q. Rate controlling mechanisms in hot deformation of 7A55 aluminum alloy. *Trans. Nonferrous Met. Soc. China* **2014**, *24*, 28–35. [[CrossRef](#)]

Disclaimer/Publisher’s Note: The statements, opinions and data contained in all publications are solely those of the individual author(s) and contributor(s) and not of MDPI and/or the editor(s). MDPI and/or the editor(s) disclaim responsibility for any injury to people or property resulting from any ideas, methods, instructions or products referred to in the content.